*J Mater Sci* (2019) 54:11056–11068

Composites

# Polyamide 66 and amino-functionalized multi-walled carbon nanotube composites and their melt-spun fibers

Jiao Zhang[1,2], Xuefeng Gao[1,2], Xianye Zhang[1,2], Haihui Liu[1,2], Hua Zhang[1,2], and Xingxiang Zhang[1,2,*]

[1] Tianjin Municipal Key Lab of Advanced Fiber and Energy Storage Technology, Tianjin 300387, China
[2] School of Material Science and Engineering, Tianjin Polytechnic University, Tianjin 300387, China

**Received:** 4 December 2018
**Accepted:** 10 April 2019
**Published online:** 13 May 2019

© Springer Science+Business Media, LLC, part of Springer Nature 2019

## ABSTRACT

A series of polyamide 66 (PA66) and multi-walled carbon nanotube (MWNT) composites were condensed using amino-functionalized MWNTs (AMWNTs), hexanediamine adipate salts, and adipic acid as raw materials. The covalent grafting of maleic acid diamine onto the surfaces of the MWNTs by a Diels–Alder reaction prevented the AMWNTs from suffering entanglement, and facilitated excellent dispersion of AMWNTs in the PA66 matrix. Analyses revealed not only that the AMWNTs are uniformly dispersed in the PA66 matrix, but also that a strong interfacial interaction exists between the AMWNTs and the matrix. An AMWNT loading of only 0.5 wt% ensured a maximum dispersibility of AMWNTs in the PA66 matrix, which was far better than that of MWNTs. Additionally, the crystallization and melting behavior of PA66/AMWNT (PACNT) composite fibers were characterized. Finally, mechanical testing results demonstrated that the Young's modulus and tensile strength of the composite fiber with 0.5 wt% AMWNT loading were increased by about 384% and 140%, respectively, compared with those of the pure PA66 fiber. Therefore, the proposed PACNT composite fibers are promising for high-performance applications.

## Introduction

With the development of nanoscience and nanotechnology, composites of polymers and nanofillers and other hybrid materials have attracted increasing attention in the fields of academia and industry [1]. The addition of nanofillers has been demonstrated to improve the structural and mechanical properties of polymer matrices without affecting their primary chemical characteristics. Among the most commonly employed nanofillers, multi-walled carbon nanotubes (MWNTs) have been shown to improve polymer composite performance significantly owing to their excellent mechanical properties and their large aspect ratio [2, 3]. However, the compatibility of MWNTs with common solvents and polymers is generally poor, and MWNTs suffer from severe entanglement due to van der Waals forces. Therefore, ensuring that

Address correspondence to E-mail: zhangpolyu@aliyun.com


https://doi.org/10.1007/s10853-019-03619-0

MWNTs are homogeneously dispersed in polymer matrices and that they have strong interfacial interactions with the matrix represents the greatest challenge for the fabrication of high-performance polymer/MWNT composites [4].

Diverse chemical surface modification methods have been developed to resolve these problems [5–7]. Unfortunately, most of the various methods presently available for the covalent functionalization of MWNTs require relatively demanding reaction conditions and several synthetic steps, which tend to damage the structure of MWNTs and suffer from relatively high complexity. In contrast, the Diels–Alder (DA) reaction employs mild, catalyst-free reaction conditions in a benign solvent-like water and generally provides a high reaction rate [8–11]. In addition, several methods have been developed for fabricating composites of polymers with functionalized MWNTs, such as melt-mixing [12–14], solution-mixing [15], and in situ polymerization [16–18]. Of these methods, in situ polymerization tends to provide better MWNT dispersion than melt-mixing by first dispersing the functionalized MWNTs in the monomers of the matrix material and then conducting polymerization with the modified monomers. Accordingly, covalent bonding can be formed between the functionalized MWNTs and the polymer matrix, resulting in composites with strong interfacial bonds that provide improved mechanical properties.

Of the many polymer materials that can be employed in the fabrication of polymer/MWNT composites, polyamide 66 (PA66) is a particularly important thermoplastic engineering material that is used in products ranging from passenger car tire cords, sporting goods, daily necessities, and rope fibers due to its excellent physical–mechanical properties [19–21]. However, the mechanical properties of PA66 limit its application in some areas, such as in aerospace, cargo truck tire cordage, and special types of high-strength engineering applications. Therefore, attempts have been made to improve the mechanical properties of PA66 through the addition of MWNTs as a reinforcing nanofiller [22–25]. For example, single-walled nanotubes (SWNTs) have been functionalized with sulfuric and nitric acids to form carboxylic SWNTs, and further reacted with thionyl chloride ($SOCl_2$) to transform –COOH groups into –COCl groups, and then reacted with dodecylamine to form amino-functionalized SWNTs, which were then finally polymerized with dichloric acid adipoyl chloride and 1,6-hexamethylene diamine in situ to fabricate PA66/SWNT composites [26]. However, this is a complex and time-consuming process requiring greater than 108 h. Similarly, MWNTs were subjected to chlorination with chlorine at 400 °C and then further reacted with a sodium hydroxide solution and ammonia to form hydroxylated MWNTs and aminated MWNTs, respectively, and the product was reacted with PA12 [27]. High temperature is required in this multi-step and complex functionalization process. Functionalized SWNTs have also been fabricated using sulfuric and nitric acid treatment, and subsequent fluorination was conducted with a fluorine, hydrogen, and helium gas-flow ratio of 2:1:30, and mixed with epoxy resin [28]. This is also a multi-step and complex process. However, while the dispersibility of the carbon nanotubes in the polymer matrix increased with the modification conducted by these multi-step processing methods, the formation of covalent bonds destroyed the $sp^2$-hybridized carbon, which negatively affected the mechanical properties of the nanotubes. Additionally, these multi-step procedures required long reaction times and were expensive and not environmentally friendly.

The present work addresses these challenges by developing a unique, simple, and efficient synthesis route for the formation of high strength PA66/MWNT composite fibers. The DA reaction served as the inspiration for applying maleic acid diamine (MAD) to provide amino-functionalized MWNTs (AMWNTs), and the developed AMWNTs facilitated the interfacial adhesion of the MWNTs with the PA66 matrix and enhanced their compatibility. To the best of our knowledge, the proposed functionalization of MWNTs, as well as the proposed fabrication of PA66/AMWNT (PACNT) composites by in situ polymerization, have been not yet been reported. The prepared PACNT composites are subjected to intensive investigation, which includes their physical and chemical properties as a function of AMWNT loading. In addition, the crystallization and melting behavior of PACNT composite fibers are characterized, and their mechanical properties are evaluated in detail.

## Experimental

### Materials

Hexanediamine adipate salt was obtained from Beijing Jinjingle Co. Adipic acid was purchased from Tianjin Fuchen Co., Ltd. We purchased MWNTs from Beijing Deke Daojin Co., Ltd. with a diameter < 8 nm, lengths from 0.5 to 2 μm, and a purity of greater than 95 wt%. We purchased MAD from TCI Huacheng Industrial Development Co., Ltd. Sulfuric acid ($H_2SO_4$, 98%), tetrahydrofuran ($C_4H_8O$, THF), formic acid (HCOOH), *N*,*N*-dimethylformamide ($C_3H_7NO$, DMF), *N*,*N*-dimethylacetamide ($CH_3C(O)N(CH_3)_2$, DMAc), dimethyl sulfoxide ($(CH_3)_2SO$, DMSO), methanol ($CH_3OH$), and dichloromethane ($CH_2Cl_2$, DCM) were purchased from Tianjin Fengchuan Reagents Co., Ltd.

### Amidation of MWNTs

We added MAD (10 g) and MWNTs (1 g) into a three-neck round-bottom flask, and the mixture was transferred to an oil bath at 190 °C with stirring for 12 h. The product was diluted with 200 mL of DMF, filtered, and the mixture was boiled for 3 h at 60 °C. This process was repeated 3 times. Subsequently, the process was repeated 6 times with water rather than DMF to ensure that the excess MAD was completely removed. The products were dried at 100 °C overnight in a vacuum oven.

### Fabrication of PACNT composites

The typical procedure for fabricating PACNT composites with 0.1 wt% AMWNT loading is depicted as follows. Hexanediamine adipate salts (40 g) and AMWNTs (0.04 g) were ground together in an agate mortar. The mixture was added into a three-neck round-bottom flask, purged with nitrogen to remove air, and the mixture was heated to 180–185 °C in an oil bath under a nitrogen atmosphere. After 1 h, the temperature of the oil bath was increased to 210–220 °C. After approximately 2 h, the temperature of the oil bath was increased to 270–280 °C, and, after approximately 4 h, the flask was cooled to room temperature. A hard block of PACNT composite material was obtained and was crushed into small pieces and washed three times in boiling water for 3 h to remove monomer and low molecular weight oligomers completely. The PACNT composites were soaked in formic acid to remove free PA66 (FRPA66) that had not grafted to the AMWNTs to obtain purified PA66-grafted AMWNTs (PPAA). This procedure was employed to obtain PACNT composites with different AMWNT loadings of 0.1, 0.3, 0.5, and 1.0 wt%, and pure PA66 was synthesized using the same engineering parameters. The corresponding nanocomposite samples are denoted herein as PACNTs-0.1, PACNTs-0.3, PACNTs-0.5, PACNTs-1.0, and PA66, respectively. In addition, the FRPA66 was collected by precipitation in water. The obtained nanocomposite samples are denoted herein as FRPA66-0.1, FRPA66-0.3, FRPA66-0.5, and FRPA66-1.0, respectively.

### Melt-spun PACNT composite fibers

Fibers of the PACNT nanocomposites were fabricated by a melt-spinning process with a custom-made piston spinning machine. All powders were maintained at 280 °C for 5 min and then melt-spun with a 0.3-mm-diameter spinneret. The as-spun PACNT composite fibers were stretched by a factor of 3.5 in hot water at 95 °C, and heat set with a hot roller at 130 °C for 2 min.

### Characterization

Fourier transform infrared (FTIR) spectroscopy was conducted using a spectrometer (Bruker TERSOR 37, Germany) in the range of 4000–500 $cm^{-1}$. The resolution was 4 $cm^{-1}$.

Micro-Raman mapping spectra were recorded on a Renishaw InVia Raman microscope (XploRA PLUS, Japan) equipped with a 532 nm laser and a Horiba Jobin–Yvon XploRA confocal Raman microscope equipped with a 532 nm laser.

X-ray photoelectron spectroscopy (XPS) measurements were taken using a spectrometer (Genesis 60, Edax, USA) equipped with an Al $K\alpha$ radiation source ($h\nu$ = 1486.4 eV).

Thermal gravimetric analysis (TGA) was conducted on a thermo-gravimetric analyzer (NETZSCH STA409PC, Germany) in the range of 40–800 °C at a heating rate of 10 °C/min under a nitrogen atmosphere.

Thermal property measurement was conducted using differential scanning calorimetry (DSC, NETZSCH DSC 200 F3, Germany). The determination

temperature varied from 0 to 350 °C at a heating or cooling rate of ± 10 °C/min under a nitrogen atmosphere (0.2 MPa) in the first cycle to remove thermal history, and the data were collected using a heating rate of 10 °C/min in a nitrogen atmosphere in the second cycle.

The molecular weight of FRPA66 and FRPA66 with various AMWNTs was expressed through the relative viscosity $\eta_r$ using

$$M_\eta = 13870 \times (\eta_r - 1.4549), \quad [29] \qquad (1)$$

where $\eta_r$ was measured at a sample concentration of 0.01 g $mL^{-1}$ in $H_2SO_4$ with an Ubbelohde viscometer at 20 °C.

X-ray diffraction (XRD, Rigaku D/MAX-2500 X-gA, Japan) was performed with filtered CuKα radiation ($\lambda$ = 0.15406 nm). Diffractograms were obtained in the 2$\theta$ range of 3° to 40° with a scan rate of 8°/min at room temperature.

Dynamic mechanical analysis (DMA, NETZSCH DMA 242, Germany) of the samples was conducted in a nitrogen atmosphere at a heating rate of 3 °C/min and a frequency of 1 Hz.

Scanning electron microscopy (SEM) was performed on a field emission SEM system (Hitachi S-4800, Japan) with an accelerating voltage of 10 kV.

Tensile testing of the fibers was conducted using an electronic tensile strength tester (LLY-06, Laizhou, China). The testing employed a fiber length of 10 mm at a tensile rate of 10 mm/min. The final results cited are the average and standard deviation values obtained from 10 samples.

## Results and discussion

### Formation mechanism of PACNT composites

The proposed formation mechanism of the PACNT composites can be summarized as follows. During the pre-polymerization process, the elevated temperature initiated a partial melting of the hexanediamine adipate salts, and polymeric chains of PA66 subsequently step-propagated with the consumption of monomers. Condensation reactions occurred between the carboxylic acid groups of the adipate acid and the amino groups of the AMWNTs, and PA66 was grafted onto the surfaces of the AMWNTs simultaneously. In addition, the viscosity of the composites increased gradually with the continuous propagation of polymer chains at high temperature, which is indicative of the high molecular weight of PA66. During the condensation polymerization process, the amino groups on the AMWNTs disrupted the stoichiometric balance between the carboxylic acids and amino groups in the reaction system. Therefore, the molecular weight of the grafted polymer chains decreased as the concentration of AMWNTs relative to the concentration of monomers increased, which increased the amino group loading of the AMWNTs. Adipic acid is a dicarboxylic acid that contains two carboxyl groups at each end of the molecular chain and played a role in regulating the molecular weight of PA66 in the system. To solve this problem, additional adipic acid was added. The scheme of forming covalent bonds on between PA66 and AMWNTs surface is shown in Fig. 1.

The FTIR spectra of MWNTs and AMWNTs are shown in Fig. 2. The broad band at 3340 $cm^{-1}$ in the AMWNTs spectrum is assigned to N–H stretching vibrations. The bands at 2917 and 2852 $cm^{-1}$ are assigned to the dissymmetry stretching vibrations of the $CH_2$ groups in the AMWNTs. The emerging broad bands at 1631 and 1575 $cm^{-1}$ for the AMWNTs correspond to the respective stretching vibrations of C=O and the N–H of the amide functionality. The band at 1259 $cm^{-1}$ is assigned to the stretching vibrations of C–N. The FTIR results indicate the existence of MAD grafted onto the MWNTs.

Figure 3 presents the Raman spectroscopy results for the MWNTs and AMWNTs. The D-band is associated with defects in the hexagonal framework of the MWNT walls, while the G-band is related to the $sp^2$-hybridized carbon framework [30]. The intensity ratio of the D and G bands of the MWNTs ($I_D/I_G$) is an indication of the degree of covalent functionalization [8, 31]. Here, the value of $I_D/I_G$ for the MWNTs was about 0.69, while that for the AMWNTs was about 0.91. Clearly, the value of $I_D/I_G$ increased after functionalization, and the carbon nanotube sidewalls included more $sp^3$ hybridized carbon atoms. However, the functionalization resulted in only a very small increase in $I_D/I_G$. The Raman results indicate that MAD has been covalently attached to the MWNTs successfully.

Generally, XPS can provide information regarding the chemical state of materials at the surface and is widely employed for chemical analysis [32]. Full-scale XPS spectra of the MWNTs and AMWNTs are

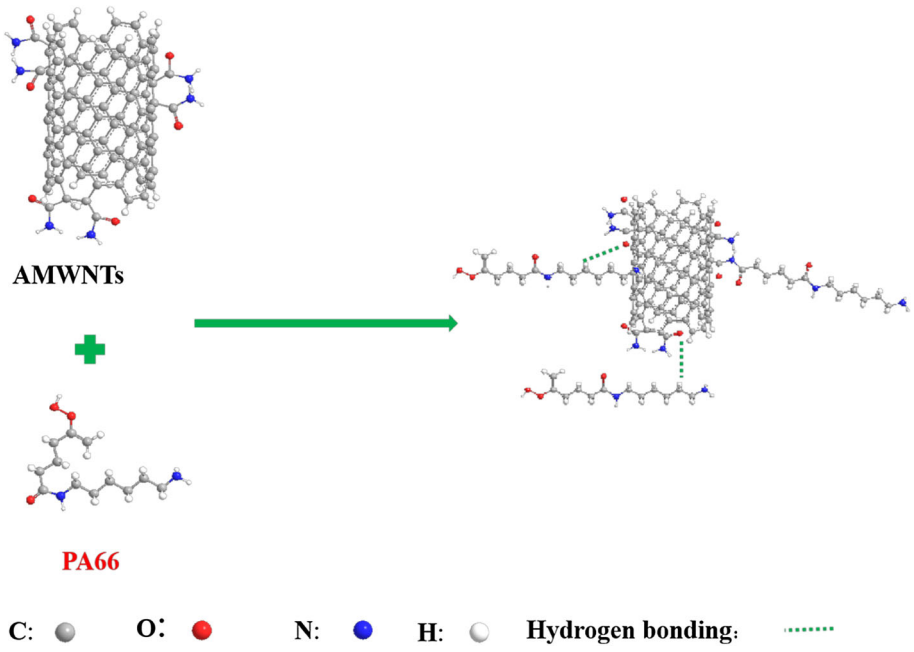


**Figure 1** The scheme of forming covalent bonds on between PA66 and AMWNTs surface.

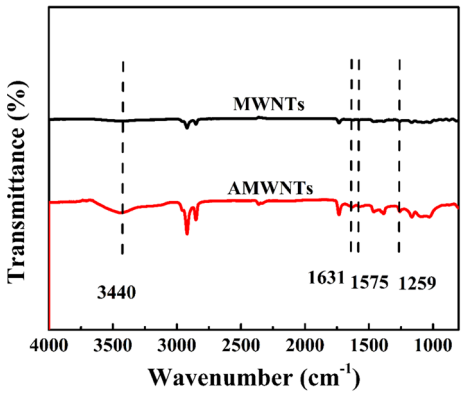


**Figure 2** FTIR spectra of MWNTs and AMWNTs.

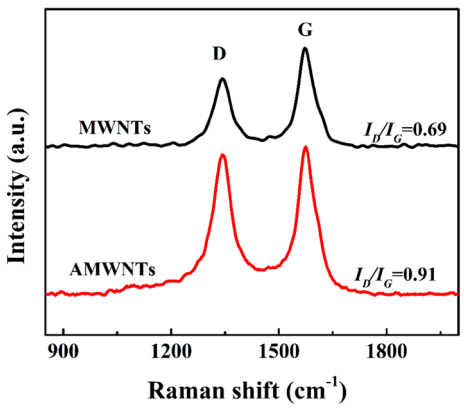


**Figure 3** Raman spectra of MWNTs and AMWNTs.

shown in Fig. 4. In the MWNTs spectrum, two obvious peaks are observed at 285.1 eV (C 1*s*) and

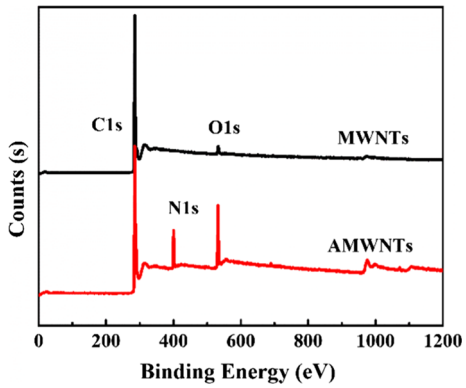


**Figure 4** Full-scale XPS spectra of MWNTs and AMWNTs.

533.0 (O 1*s*) [33], and no peak indicative of nitrogen was detected. For the AMWNTs spectrum, an N 1*s* signal was detected at 400.1 eV in addition to C 1*s* and O 1*s* signals, which indicates that MAD was grafted onto the MWNTs successfully. As shown in Fig. 4, the C 1*s* spectra of the MWNTs and AMWNTs were convoluted because parts of the unwashed composites were coated with carbon nanotubes. Therefore, the C 1*s* spectrum was deconvolved to obtain a number of peaks that can be assigned to various bonds. The C 1*s* spectra of the MWNTs and the AMWNTs are shown in Fig. 5. The C 1*s* peak of the MWNTs can be deconvoluted into three peaks with binding energies of 284.6, 285.5, and 290.5 eV, which are assigned to C = C, C–C, and O–C=O states, respectively [34]. In addition to these deconvoluted

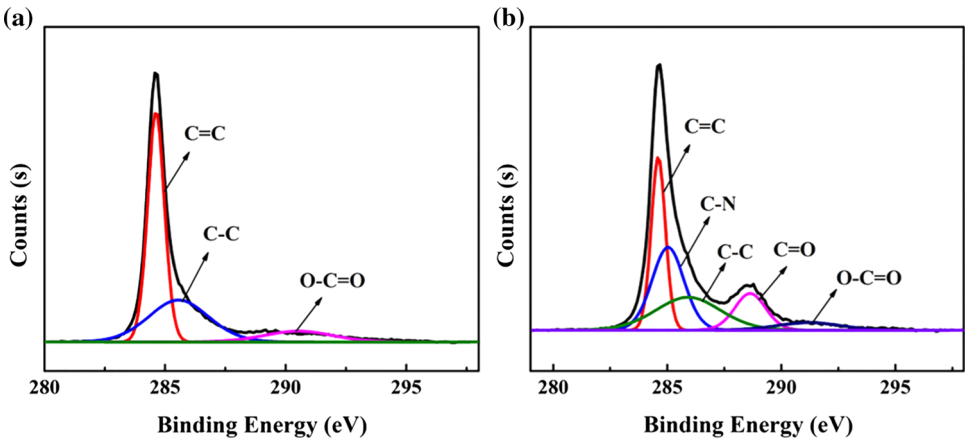


**Figure 5** C 1*s* spectra of **a** MWNTs and **b** AMWNTs.

peaks, the C 1*s* peak of the AMWNTs could be deconvoluted into C–N and C=O components at binding energies of 285.0 and 288.6 eV, respectively, which further confirms that MAD was successfully grafted onto the surface of the MWNTs. These results are therefore consistent with the results obtained via the above analysis of the FTIR and Raman spectra.

The dispersion of the AMWNTs and MWNTs in the PA66 matrix was investigated based on the Hildebrand solubility parameter ($\delta$). The value of $\delta$ is derived directly from the cohesive energy density (CED) as follows:

$$\delta = (E/V)^{1/2}. \tag{2}$$

here $E$ is the molar cohesive energy and $V$ is the molar volume of the solvent. According to Hansen's theory [35], the CED of any material is the sum of Hansen dispersion ($d$), polarity ($p$), and hydrogen bonding ($h$) components. As such, the CED consists of three components:

$$\mathrm{CED} = E/V = E_d/V + E_p/V + E_h/V. \tag{3}$$

This leads to three solubility parameters, where each is equal to the square root of the associated CED. Thus, the sum of the squares of these Hansen solubility parameters equals the square of the Hildebrand solubility parameter:

$$\delta^2 = \delta_d^2 + \delta_{p+}^2 \delta_h^2. \tag{4}$$

The three Hansen solubility parameters are then given as follows:

$$\delta_i = \sum_{\text{solvent}} C\,\delta_{i,\text{sol}} / \sum_{\text{solvent}} C \quad (i = d, p, h), \tag{5}$$

where $C$ is the dispersability in a given solvent and $\delta_{i.\text{sol}}$ is the $i$th Hansen solubility parameter in a given solvent.

According to the Lambert–Beer law ($A = \alpha \cdot C \cdot L$, where $A$ is the absorbance, $\alpha$ is the absorption coefficient, $C$ is the concentration of the dispersant, and $L$ is the thickness of the liquid layer) and previous research [36], the three Hansen parameters in Eq. (2) can be simplified as follows.

$$\delta_i = \sum_{\text{solvent}} A\delta_{i,\text{sol}} / \sum_{\text{solvent}} A \tag{6}$$

The solubility parameters of various solvents are listed in Table 1. The values of $\delta_d$, $\delta_p$, and $\delta_h$ obtained with Eq. (6) using a series of good solvents for AMWNTs can therefore be given as 17.0, 12.2, and 10.6 $\text{MPa}^{1/2}$, respectively. Accordingly, the value of $\delta$ for AMWNTs can be calculated from Eq. (4) as 23.5 $\text{MPa}^{1/2}$. Employing the same method for calculating the values of $\delta_d$, $\delta_p$, and $\delta_h$ for MWNTs yielded 17.2, 10.5, and 10.0 $\text{MPa}^{1/2}$, respectively, and the value of $\delta$ calculated by Eq. (4) was 22.5 $\text{MPa}^{1/2}$. The Hansen parameters for PA66 in an equivalent solvent ($\delta_d$ = 17.4 $\text{MPa}^{1/2}$, $\delta_p$ = 9.80 $\text{MPa}^{1/2}$, and $\delta_h$ = 14.6 $\text{MPa}^{1/2}$) were obtained from the literature [35], and the calculated value of $\delta$ was 24.7 $\text{MPa}^{1/2}$. These results indicate that the value of $\delta$ for the AMWNTs is closer to that of PA66. As such, the dispersibility of the AMWNTs in the PA66 matrix is expected to be better than that of MWNTs according to the principle of like dissolves like. Therefore, we can expect that the strength and Young's modulus of the resulting PACNT composites will be enhanced.

**Table 1** Hansen parameters of various solvents

| Solvents | Molecular formula | $\delta_d$ (MPa$^{1/2}$) | $\delta_p$ (MPa$^{1/2}$) | $\delta_h$ (MPa$^{1/2}$) | $\delta$ (MPa$^{1/2}$) |
|---|---|---|---|---|---|
| DMF | $HCON(CH_3)_2$ | 17.4 | 13.7 | 11.3 | 26.6 |
| DMSO | $(CH_3)_2SO$ | 18.4 | 16.4 | 10.2 | 26.7 |
| DMAc | $CH_3C(O)N(CH_3)_2$ | 16.8 | 11.5 | 10.2 | 22.8 |
| THF | $C_4H_8O$ | 16.8 | 5.7 | 8.0 | 19.4 |
| Methanol | $CH_3OH$ | 15.1 | 12.3 | 22.3 | 29.6 |
| Formic acid | HCOOH | 14.3 | 11.9 | 16.6 | 24.9 |
| DCM | $CH_2Cl_2$ | 18.2 | 6.3 | 6.1 | 20.2 |

## Thermal properties of PACNT composites

The TGA and DTG curves of PA66 and the PACNT composites with various AMWNT loadings are shown in Fig. 6a, b, respectively. Pure PA66 shows a $T_{5\%}$ of 378 °C, and the major mass loss of PA66 is observed in the temperature range 381–500 °C, which is due to the decomposition of macromolecular chains. A similar result was reported for nano-hydroxyapatite-PA66 [37]. $T_{max}$ are denoted to the maximum mass temperature. Figure 5b shows that $T_{max}$ of all PACNT composites is high than PA66.

## Melting and crystallization behavior of PACNT composites

Crystallization has an extreme effect on the properties of composites involving crystalline polymers. The crystalline structures of PA66 can be divided into two primary phases, including the triclinic α-crystalline phase and the pseudo-hexagonal γ-crystalline phase. The α phase is composed of stacked planar sheets of hydrogen bonded chains with the sheets displaced along the chain direction by a fixed amount. The γ phase has pleated sheets of methylene units with hydrogen bonding between the sheets rather than within the sheets [38]. The α phase of PA66 is much more stable than the γ phase at room temperature. As reported by Bell et al. [39], PA66 exhibits two melting peaks that may appear individually or together, depending on annealing and stretching conditions. Here, the DSC heating curves given in Fig. 7a indicate that all samples in the present system have only a single melting peak. Moreover, the pure PA66 exhibited a melting temperature ($T_m$) of 269.2 °C, which corresponds to the α-crystalline phase. We also note from Fig. 7a that the values of $T_m$ for the PACNT composites shifted to lower temperatures than that of the pure PA66 with increasing AMWNT loading. We propose that the reason for this decrease is that the molecular weight of the polymer decreases with increasing AMWNT loading. To confirm this proposal, we investigated the TGA curves of PPAA with various AMWNT loadings shown in Fig. 8 and evaluated the molecular weights of PA66 and FRPA66 with various AMWNT loadings, which are listed in Table 2. The TGA mass data decreased with increasing AMWNT loading, as shown in Fig. 8. As such, the amount of PA66 grafted onto the AMWNTs decreased with increasing AMWNT loading, and Table 2 shows that the molecular weights of the free PA66 samples decreased with increasing AMWNT loading from 26500 for pure PA66 to 10300 g mol$^{-1}$ for PACNTs-1.0. We note that these results support

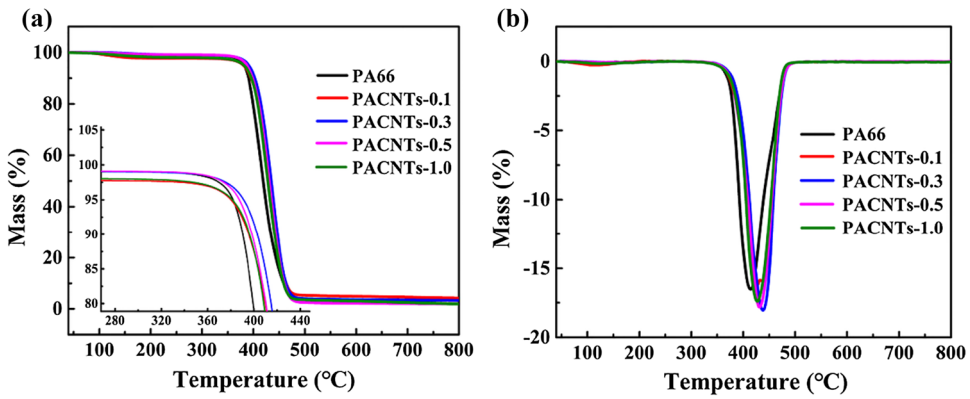


**Figure 6** **a** TGA and **b** DTG curves of PA66 and the PACNT composites with various AMWNT loadings.

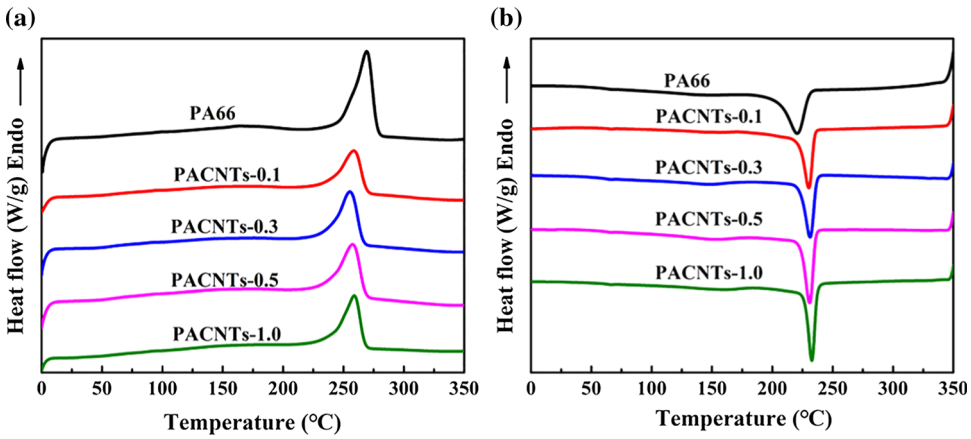


**Figure 7** DSC **a** heating and **b** cooling curves of PACNT composites with various AMWNT loadings.

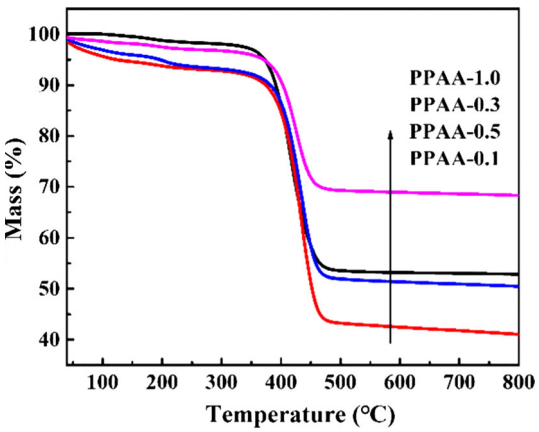


**Figure 8** TGA curves of PPAA with various AMWNT loadings.

**Table 2** Molecular weights of PA66 and FRPA66 with various AMWNT loadings

| Samples | Relative viscosity | $M_\eta$ (g mol$^{-1}$) |
|---|---|---|
| PA66 | 3.36 | $2.65 \times 10^4$ |
| FRPA66-0.1 | 3.01 | $2.17 \times 10^4$ |
| FRPA66-0.3 | 2.57 | $2.12 \times 10^4$ |
| FRPA66-0.5 | 2.47 | $1.41 \times 10^4$ |
| FRPA66-1.0 | 2.20 | $1.03 \times 10^4$ |

the above proposal well. The same phenomenon was also reported by Zhou et al. [36]. The crystallization temperature ($T_c$) of pure PA66 appears at 220.6 °C, as indicated by the DSC cooling curves in Fig. 7b, and the values of $T_c$ for the PACNT composites shifted toward higher temperature and the widths of the crystalline peaks became increasingly narrow with increasing AMWNT loading. These results indicate that the AMWNTs increase the crystallization rate of the composites and have a strong hetero-nucleation effect on the PA66 matrix. It is also known that the value of $T_c$ for composites increases with the introduction of clay and carbon nanotubes [38, 40, 41].

We also investigated the effect of AMWCNT loading on the crystallinity of the PA66 matrix by evaluating the degree of crystallization ($X_c$) of the PACNT composites using the following relationship:

$$X_c(\%) = \Delta H_c \times 100/\Delta H_c^0, \quad (7)$$

where $\Delta H_c$ is the heat of crystallization for the PACNT composites and $\Delta H_c^0$ is the heat of crystallization for 100% crystalline PA66, which is 188 J/g [42]. For comparison, the values of $\Delta H_c$ and $X_c$ for PA66 and the PACNT composites are also listed in Table 3. These results demonstrate that the addition of AMWNTs leads to increase in $X_c$, where $X_c$ reaches a maximum for an AMWNT loading of 0.5 wt%, but decreases with the further addition of AMWNTs. The main reason for this crystallization behavior is that the AMWNTs have two contradictory influences on the crystallization of semicrystalline polymers. On the one hand, they act as heterogeneous nucleating agents to facilitate the crystallization of polymers, while, on the other hand, AMWNTs hinder the motion of polymer chain segments, thereby retarding the crystallization of polymers [43]. This confinement effect eventually

**Table 3** Crystallization parameters of PA66 and PACNT composites

| Samples | $T_m$ (°C) | $T_c$ (°C) | $\Delta H_c$ (J g$^{-1}$) | $X_c$ (%) |
|---|---|---|---|---|
| PA66 | 269.2 | 220.6 | 59.70 | 31.76 |
| PACNTs-0.1 | 258.7 | 230.2 | 60.31 | 32.08 |
| PACNTs-0.3 | 255.4 | 231.3 | 75.89 | 40.37 |
| PACNTs-0.5 | 257.6 | 230.9 | 86.04 | 45.77 |
| PACNTs-1.0 | 258.9 | 232.7 | 66.03 | 35.12 |

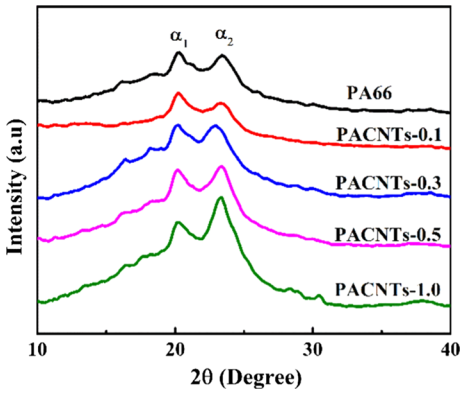


**Figure 9** XRD patterns of PA66 and the PACNT composites.

outweighs the nucleation effect and decreases the overall crystallization kinetics.

The XRD patterns of PA66 and the PACNT composites are presented in Fig. 9. The two strong diffraction peaks at 20.29° and 23.41° correspond to the (100) and (010) crystal planes, respectively, which are, respectively, defined as $\alpha_1$ and $\alpha_2$ [38]. The (100) crystal planes corresponding with the $\alpha_1$ peak represent the stacked planar sheets of the hydrogen-bonded chains associated with the α phase of PA66, and the (010) crystal planes corresponding with the $\alpha_2$ peak arise from the hydrogen-bonded pleated sheets associated with the α phase of PA66 [44]. The sharp decrease in the intensity of the $\alpha_1$ peak for the PACNT composites indicates that the addition of AMWNTs disturbs the perfect arrangement of the hydrogen-bonded chains of the α phase. Therefore, it is reasonable to ascribe this phenomenon to an interaction between the AMWNTs and the polymer chains. Moreover, the intensity of the $\alpha_1$ peak of the composites decreases proportionally with increasing AMWNT loading, and the corresponding increasing intensity of the $\alpha_2$ peak is not proportional to the AMWNT loading. This indicates that the AMWNTs have a strong hetero-nucleation effect on the PA66 matrix. The crystallite sizes ($D$) of PA66 and the PACNT composites can be determined from the XRD data according to the Scherrer expression:

$$D = K\lambda/\beta\cos\theta, \tag{8}$$

where $K$ is the Scherrer factor ($K$ = 0.9), $\lambda$ is the X-ray wavelength ($\lambda$ = 0.15406 nm), $\beta$ is the measured full-width at half maximum of the respective peak, and $\theta$ is its Bragg angle. The values of $D$ calculated using Eq. (8) are listed in Table 4. We note that $D$(100) decreased with an increasing AMWNT loading because of the suppressed crystal growth caused by interactions between the AMWNTs and the PA66 matrix. In addition, no linear relationship was obtained between $D$(010) and the AMWNT loading.

**Table 4** Crystallite sizes of PA66 and the PACNT composites obtained from Fig. 8 and Eq. (8)

| Samples | 2θ | | $D$ (100) | $D$ (010) |
|---|---|---|---|---|
| | $\alpha_1$ | $\alpha_2$ | (nm) | (nm) |
| PA66 | 20.29 | 23.41 | 9.9 | 8.4 |
| PACNTs-0.1 | 20.20 | 23.40 | 10.1 | 8.0 |
| PACNTs-0.3 | 20.19 | 22.90 | 9.7 | 7.8 |
| PACNTs-0.5 | 20.19 | 23.40 | 9.6 | 8.5 |
| PACNTs-1.0 | 20.20 | 23.39 | 9.3 | 8.5 |

## Dynamic mechanical properties of PACNT composites

Figure 10a, b presents the loss factor (tan $\delta$) and storage modulus ($E'$) curves of the PACNT composites, respectively. In addition, the temperatures corresponding to the tan $\delta$ peaks can be taken as the glass transition temperature ($T_g$). Accordingly, the DMA parameters are listed in Table 4. The greater value of $E'$ obtained for PACNTs-0.5 than that of PA66 is representative of an increased stiffness and load-bearing capacity of the composite. This significant improvement can be attributed to the fine dispersion of AMWNTs in the PA66 matrix and the formed covalent linkages between the AMWNTs and the matrix [17]. Another important feature is that the tan $\delta$ peaks for the PACNT composites shifted toward higher temperature relative to that of PA66, as shown in Fig. 10a. It is well known that the $T_g$ value of the polymer matrix in composites depends on the free volume of the polymer, which is related to the affinity between the filler and the polymer matrix [24, 45, 46]. From Table 5, we note that the $T_g$ values for the PACNT composites are all greater than that of PA66, which indicates that the AMWNTs have good dispersion and a strong affinity with the PA66 matrix. As a result, the free volume of the corresponding composites decreases and $T_g$ increases [23]. Moreover, the tan $\delta$ values decreased markedly with the addition of AMWNTs, indicating that the movement of the PA66 molecular chains was constrained substantially by the AMWNTs.

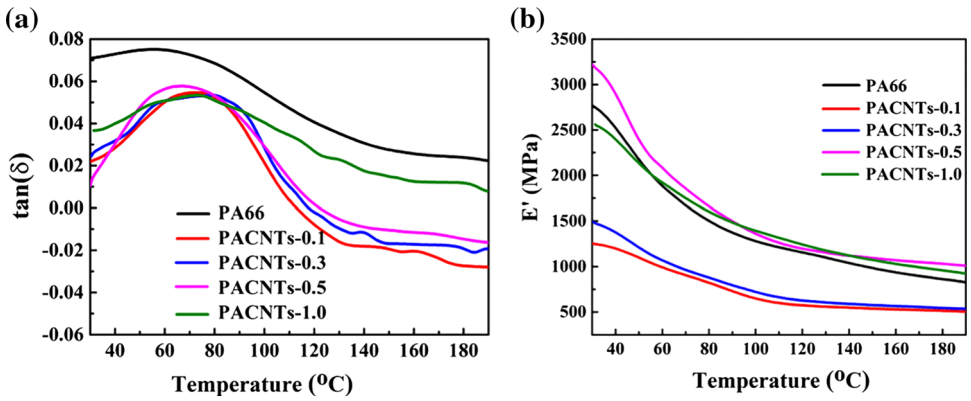


**Figure 10** Values of **a** tan $\delta$ and **b** storage modulus ($E'$) as a function of temperature for PA66 and the PACNT composites.

## PACNT composite fibers

Figure 11 presents SEM micrographs of the fracture surfaces of PACNT composite fibers. Here, the white dots or rods in the micrographs represent the broken ends of AMWNTs. It is readily observed from Fig. 11d that the AMWNTs in PACNTs-1.0 undergo significant agglomeration. However, Fig. 11a–c shows that the AMWNTs in PACNTs-0.1, PACNTs-0.3, and PACNTs-0.5 are uniformly dispersed in the PA66 matrix and that the PA66 forms a surrounding cladding layer that firmly entraps the AMWNTs. Moreover, an AMWNT loading of 0.5 wt% demonstrates a greater dispersibility and stronger interfacial interaction with the PA66 matrix than the other AMWNT loadings. This indicates that strong chemical bonds are formed between the AMWNTs and PA66 in this case. The stress on the PA66 matrix is thereby transferred to the AMWNTs effectively, and this restricts the movement of the PA66 molecular chains.

**Table 5** DMA parameters of PA66 and the PACNT composites

| Samples | $E'$ (MPa) | $T_g$ (°C) | tan $\delta$ |
|---|---|---|---|
| PA66 | 2778.61 | 55.5 | 0.075 |
| PACNTs-0.1 | 1255.75 | 73.3 | 0.055 |
| PACNTs-0.3 | 1490.89 | 79.4 | 0.053 |
| PACNTs-0.5 | 3224.23 | 62.9 | 0.057 |
| PACNTs-1.0 | 2561.39 | 72.8 | 0.053 |

The physical–mechanical properties of the PACNT composite fibers with various AMWNT loadings are

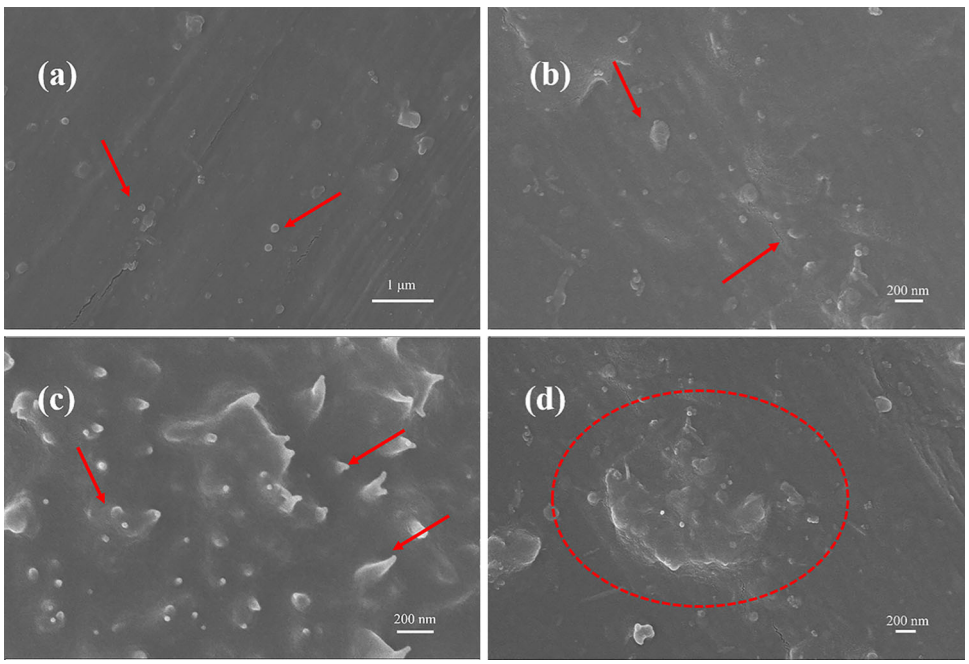


**Figure 11** SEM micrographs of the fracture surfaces of PACNT composite fibers: **a** PACNTs-0.1, **b** PACNTs-0.3, **c** PACNTs-0.5, **d** PACNTs-1.0.

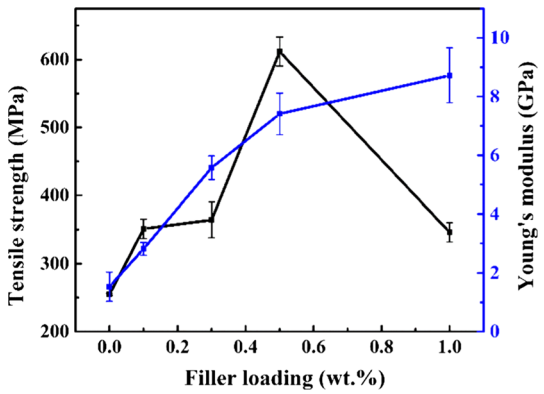


**Figure 12** Tensile strength and Young's modulus of PACNT composite fibers with various AMWNT loadings.

presented in Fig. 12. It can be seen that, with increasing AMWNT loading, the tensile strength of the composite fibers first increases, reaches a maximum at an AMWNT loading of 0.5 wt%, and then decreases, but the Young's modulus of the composites increases continuously with increasing AMWNT loading. Compared with pure PA66, the addition of only 0.5 wt% AMWNTs increased the tensile strength by roughly 140% from 255 to 611 MPa, while the Young's modulus increased by 384%, which clearly demonstrates the significant reinforcing effect of AMWNTs on the PA66 matrix. The tensile strength and Young's modulus results obtained here are the greatest among all previously published reports of PA66 composites [47–51].

Based on these results, we propose the following two factors for explaining the superior mechanical properties of the PACNT composites. The surface modification of the MWNTs by the grafting of MAD leads to an increased interlayer distance between the MWNTs that prevents their restacking and also ensures the preservation of an intact MWNT structure during processing. The AMWNT surfaces provide amino groups for grafting to PA66 directly via in situ polymerization, and this leads to the formation of strong interfacial interactions between the AMWNTs and the PA66 matrix.

## Conclusions

The present work demonstrated the effective grafting of MAD on the surfaces of MWNTs through a DA reaction, which is a relatively mild and rapid process. The chemical bonds formed between the MAD molecular chains prevented the AMWNTs from suffering entanglement. As a result, the dispersion of AMWNTs in the PA66 matrix was better than that of MWNTs. The Young's modulus and tensile strength of PACNT composite fibers were greatly increased relative to those of a pure PA66 fiber even with a very low AMWNT loading, and maximum values were obtained for an AMWNT loading of 0.5 wt%, which represented an increase in the Young's modulus and tensile strength of about 384% and 140%, respectively, compared with the pure PA66 fiber. Therefore, the proposed PACNT composite fibers are promising for applications in high-performance tire cordage, transport belts, and rope.

## Acknowledgements

This work was supported by the National Key Research and Development Program of China (Grant No. 2016YFB0303000) and the New Materials Research Key Program of Tianjin (Grant No. 16ZXCLGX00090).

## References

[1] Kumar A, Sharma K, Dixit AR (2019) A review of the mechanical and thermal properties of graphene and its hybrid polymer nanocomposites for structural applications. J Mater Sci 54:5992–6026. https://doi.org/10.1007/s10853-018-03244-3

[2] Bai YX, Zhang RF, Ye X et al (2018) Carbon nanotube bundles with tensile strength over 80 GPa. Nat Nanotechnol 13:589–595. https://doi.org/10.1038/s41565-018-0141-z

[3] Sharma K, Shukla M (2014) Molecular modeling of the mechanical behavior of carbon fiber-amine functionalized multiwall carbon nanotube/epoxy composites. New Carbon Mater 29(2):132–142

[4] Tasis D, Tagmatarchis N, Bianco A, Prato M (2006) Chemistry of carbon nanotubes. Chem Rev 106:1105–1136

[5] Hong CY, You YZ, Pan CY (2006) A new approach to functionalize multi-walled carbon nanotubes by the use of functional polymers. Polymer 47:4300–4309

[6] Mohammad M, Winey KI (2006) Polymer nanocomposites containing carbon nanotubes. Macromolecules 39:543–545

[7] Gromov A, Dittmer S, Svensson J, Nerushev OA, Perez-García SA, Licea-Jiménez L, Rychwalski R, Campbell EEB (2005) Covalent amino-functionalisation of single-wall carbon nanotubes. J Mater Chem 15:3334–3339

[8] Le CMQ, Cao XT, Lim KT (2017) Ultrasound-promoted direct functionalization of multi-walled carbon nanotubes in water via Diels–Alder "click chemistry". Ultrason Sonochem 39:321–329

[9] Le CMQ, Cao XT, Jeong YT, Lim KT (2018) Covalent functionalization of multi-walled carbon nanotubes with imidazolium-based poly(ionic liquid)s by Diels–Alder "click" reaction. J Ind Eng Chem 64:337–343. https://doi.org/10.1016/j.jiec.2018.03.034

[10] Zydziak N, Hübner C, Bruns M, Barnerkowollik C (2011) One-step functionalization of single-walled carbon nanotubes (SWCNTs) with cyclopentadienyl-capped macromolecules via Diels–Alder chemistry. Macromolecules 44:3374–3380

[11] Delgado JL, Cruz PDL, Langa F, Urbina A, Casado J, López N (2004) Microwave-assisted sidewall functionalization of single-wall carbon nanotubes by Diels–Alder cycloaddition. Chem Commun 15:1734–1735

[12] Socher R, Krause B, Boldt R, Hermasch SWR, Pötschke P (2011) Melt mixed nano composites of PA12 with MWNTs: influence of MWNT and matrix properties on macrodispersion and electrical properties. Compos Sci Technol 71:306–314

[13] Wu ZG, Zhou CX, Zhu N (2002) The nucleating effect of montmorillonite on crystallization of nylon 1212/montmorillonite nanocomposite. Polym Test 21:479–483

[14] Yu ZZ, Yan C, Yang MS, Mai YW (2004) Mechanical and dynamic mechanical properties of nylon 66/montmorillonite nanocomposites fabricated by melt compounding. Polym Int 53:1093–1098

[15] Jeon HS, Rameshwaram JK, Kim G, Weinkauf DH (2003) Characterization of polyisoprene–clay nanocomposites prepared by solution blending. Polymer 44:5749–5758

[16] Xu Z, Gao C (2010) In situ polymerization approach to graphene-reinforced nylon-6 composites. Macromolecules 43:6716–6723

[17] Zeng HL, Gao C, Wang YP, Watts PCP, Kong H, Cui XW, Yan DY (2006) In situ polymerization approach to multiwalled carbon nanotubes-reinforced nylon 1010 composites: mechanical properties and crystallization behavior. Polymer 47:113–122

[18] Wang X, Kalali EN, Wang DY (2015) An in situ polymerization approach for functionalized $MoS_2$/nylon-6 nanocomposites with enhanced mechanical properties and thermal stability. J Mater Chem A 3:24112–24120

[19] Cao JS, Cheng ZQ, Kang LJ, Zhang YY, Zhao XD, Zhao SZ, Gao B (2017) Novel anti-fouling polyethersulfone/polyamide 66 membrane preparation for air filtration by electrospinning. Mater Lett 192:12–16

[20] Baji A, Mai YW, Wong SC, Abtahi M, Du XS (2010) Mechanical behavior of self-assembled carbon nanotube reinforced nylon 66 fibers. Compos Sci Technol 70:1401–1409

[21] Mirvakil SM, Hunter IW (2017) Multidirectional artificial muscles from nylon. Adv Mater 29:160–166. https://doi.org/10.1002/adma.201604734

[22] Sengupta R, Ganguly A, Sabharwal S, Chaki TK, Bhowmick AK (2007) MWCNT reinforced polyamide-66 films: preparation, characterization and properties. J Mater Sci 42:923–934. https://doi.org/10.1007/s10853-006-0011-1

[23] Zhang XX, Meng QJ, Wang XC, Bai SH (2010) Poly(adipic acid-hexamethylene diamine)-functionalized multi-walled carbon nanotube nanocomposites. J Mater Sci 46:923–930. https://doi.org/10.1007/s10853-010-4836-2

[24] Mahmood N, Islam M, As Hameed, Saeed S, Khan AN (2013) Polyamide-6-based composites reinforced with pristine or functionalized multi-walled carbon nanotubes produced using melt extrusion technique. J Compos Mater 48:1197–1207

[25] Jose MV, Steinert BW, Thomas V, Dean DR, Abdalla MA, Price G, Janowski GM (2007) Morphology and mechanical properties of nylon 6/MWNT nanofibers. Polymer 48:1096–1104

[26] Haggenmueller R, Du FM, Fischer JE, Winey KI (2006) Interfacial in situ polymerization of single wall carbon nanotube/nylon 66 nanocomposites. Polymer 47:2381–2388

[27] Pelech I, Kwiatkowska M, Jedrzejewska A, Pelech R, Kowalczyk I (2017) Thermal and mechanical properties of polyamide 12/modified carbon nanotubes composites prepared via the in situ ring-opening polymerization. Polimery-W 62:101–108

[28] Zhu J, Kim J, Peng HQ, Margrave JL, Khabashesku VN, Barrera EV (2003) Improving the dispersion and integration of single-walled carbon nanotubes in epoxy composites through functionalization. Nano Lett 3:1107–1113

[29] Li YY, Liu K, Xiao R (2017) Preparation and characterization of flame-retarded polyamide 66 with melamine cyanurate by in situ polymerization. Macromol Res 25:779–785

[30] Liu HH, Peng WW, Hou LC, Wang XC, Zhang XX (2013) The production of a melt-spun functionalized graphene/poly(ε-caprolactam) nanocomposite fiber. Compos Sci Technol 81:61–68

[31] Datsyuk V, Kalyva M, Papagelis K, Parthenios J, Tasis D, Siokou A, Kallitsis I, Galiotis C (2008) Chemical oxidation of multiwalled carbon nanotubes. Carbon 46:833–840

[32] Xiao LH, Xu LL, Yang YY, Zhang S, Huang Y, Bielawski CW, Geng JX (2017) Core–shell structured polyamide 66 nanofibers with enhanced flame retardancy. ACS Omega 2:2665–2671

[33] Cao RR, Sai Chen, Liu HB, Liu HH, Zhang XX (2017) Fabrication and characterization of thermo-responsive GO nanosheets with controllable grafting of poly(hexadecyl acrylate) chains. J Mater Sci 53:4103–4117. https://doi.org/10.1007/s10853-017-1864-1

[34] Neves JC, De Castro VG, Assis ALS, Veiga AG, Rocco MLM, Silva GG (2018) In-situ determination of amine/epoxy and carboxylic/epoxy exothermic heat of reaction on surface of modified carbon nanotubes and structural verification of covalent bond formation. Appl Surf Sci 436:495–504

[35] Hansen CM (2007) Hansen solubility parameters: a user's handbook, 2nd edn. Springer, New York

[36] Zhou LF, Liu HH, Zhang XX (2015) Poly(styrene–maleic anhydride) functionalized graphene oxide. J Appl Polym Sci 132:11–17. https://doi.org/10.1002/app.41987

[37] Zhang X, Li YB, Lv GY, Zuo Y, Mu YH (2006) Thermal and crystallization studies of nano-hydroxyapatite reinforced polyamide 66 biocomposites. Polym Degrad Stabil 91:1202–1207

[38] Liu XH, Wu QJ, Berglund LA (2002) Polymorphism in polyamide 66/clay nanocomposites. Polymer 43:4967–4972

[39] Bell JP, Slade PE, Dumbleton JH (1968) Multiple melting in nylon 66. J Polym Sci Part B Pol Phys 6:1773–1781

[40] Valentini L, Biagiotti J, López MMA, Santucci S, Kenny JM (2004) Effects of carbon nanotubes on the crystallization behavior of polypropylene. Polym Eng Sci 44:303–311

[41] Kaynak C, Sankal S (2014) Effects of oxidative functionalized and aminosilanized carbon nanotubes on the crystallization behaviour of polyamide-6 nanocomposites. Polym Bull 71:855–873

[42] Howard W, Starkweather JR, Tarkweather A, Jones EI (1981) Crystalline transitions in powders of nylon 66 crystallized from solution. J Polym Sci Pol Chem 19:467–477

[43] Qiu L, Yang YZ, Xu LH, Liu XG (2013) Influence of surface modification of carbon nanotube on microstructures and properties of polyamide 66/multiwalled carbon nanotube composites. Polym Compos 34:656–664

[44] Vasanthan N, Murthy NS, Bray RG (1998) Investigation of brill transition in nylon 6 and nylon 66 by infrared spectroscopy. Macromolecules 31:8433–8435

[45] Meng H, Sui GX, Fang PF, Yang R (2008) Effects of acid- and diamine-modified MWNTs on the mechanical properties and crystallization behavior of polyamide 6. Polymer 49:610–620

[46] Scaffaro R, Maio A (2017) A green method to prepare nanosilica modified graphene oxide to inhibit nanoparticles re-aggregation during melt processing. Chem Eng J 308:1034–1047

[47] You JW, Choi HH, Cho J, Son JG, Park M, Lee SS, Park JH (2018) Highly thermally conductive and mechanically robust polyamide/graphite nanoplatelet composites via mechanochemical bonding techniques with plasma treatment. Compos Sci Technol 160:245–254

[48] Zheng JC, Han DL, Ye X, Wu XH, Wu YP, Wang YQ, Zhang LQ (2018) Chemical and physical interaction between silane coupling agent with long arms and silica and its effect on silica/natural rubber composites. Polymer 135:200–210

[49] Kim OJ, Lee KY, Jung I, Park M (2017) Dispersion of graphene-based nanocarbon fillers in polyamide 66 by dry processing and its effect on mechanical properties. Compos Part B Eng 114:445–456

[50] Liu HH, Hou LC, Peng WW, Zhang Q, Zhang XX (2012) Fabrication and characterization of polyamide 6-functionalized graphene nanocomposite fiber. J Mater Sci 47:8052–8060. https://doi.org/10.1007/s10853-012-6695-5

[51] Chen T, Liu HH, Wang XC, Zhang H, Zhang XX (2018) Properties and fabrication of PA66/surface-modified multiwalled nanotubes composite fibers by ball milling and melt-spinning. Polymers 10:547–559. https://doi.org/10.3390/polym10050547

**Publisher's Note** Springer Nature remains neutral with regard to jurisdictional claims in published maps and institutional affiliations.